ADVANCED FUNCTIONAL MATERIALS
www.afm-journal.de

Materials Views
www.MaterialsViews.com

Low-Cost Post-Growth Treatments of Crystalline Silicon Nanoparticles Improving Surface and Electronic Properties

Sabrina Niesar, Rui N. Pereira, Andre R. Stegner, Nadine Erhard, Marco Hoeb, Andrea Baumer, Hartmut Wiggers, Martin S. Brandt,* and Martin Stutzmann*

Freestanding silicon nanocrystals (Si-ncs) offer unique optical and electronic properties for new photovoltaic, thermoelectric, and other electronic devices. A method to fabricate Si-ncs which is scalable to industrial usage has been developed in recent years. However, barriers to the widespread utilization of these nanocrystals are the presence of charge-trapping defects and an oxide shell formed upon ambient atmosphere exposure hindering the charge transport. Here, we exploit low-cost post-growth treatment routes based on wet-etching in hydrofluoric acid plus surface hydrosilylation or annealing enabling a complete native oxide removal and a reduction of the defect density by up to two orders of magnitude. Moreover, when compared with only H-terminated Si-ncs we report an enhancement of the conductivity by up to a factor of 400 for films of HF etched and annealed Si-ncs, which retain a defect density below that of untreated Si-ncs even after several months of air exposure. Further, we demonstrate that HF etched and hydrosilylated Si-ncs are extremely stable against oxidation and maintain a very low defect density after a long-term storage in air, opening the possibility of device processing in ambient atmosphere.

1. Introduction

In times of a changing energy market, it is of great interest to explore the field of cost-efficient solar cells and thermoelectric power devices that make use of semiconducting nanoscale materials.[1,2] In particular, the research on solution-processable thin films of freestanding semiconductor nanoparticles, which are also promising for other electronic devices, has extended rapidly in the last years.[3–5] Silicon nanocrystals (Si-ncs) have emerged as a particularly interesting base material for such applications due to their unparalleled physical properties[6] and the ability of upscaling their synthesis in the gas phase via a microwave plasma reactor to an industrial level.[7] Initial studies demonstrating the feasibility of silicon nanocrystal based hybrid solar cells and thermoelectric devices have shown that the achievable efficiencies are limited by transport barriers due to a native oxide shell that grows by exposure to air and a relatively high concentration of silicon dangling bond (Si-db) defects of 7×10^{11} cm^{-2} in the Si-nc networks,[4,5,8,9] which act as recombination and trapping centers.[10,11] Therefore, the reduction of the Si-db density as well as the optimization of the Si-nc surfaces for an efficient inter Si-nc charge transfer are ongoing challenges.[12–15] To keep the advantage of the large scale production of Si-ncs in a microwave plasma reactor, cost-efficient post-growth processes are desired which lower the Si-db concentration, remove the native oxide, permit the attachment of functional organic groups, and also allow the handling of the Si-ncs in air. Such a functionalization is also important for the design and optimization of hybrid inorganic-organic interfaces via covalent linker molecules, which is interesting for solar cells, biosensors, and medical applications.[16–23]

Here, we demonstrate a strong reduction of the number of Si-db defects for a large range of Si-nc diameters via different post-growth treatments. Our work focuses on HF etching in conjunction with low-temperature vacuum annealing at 200 °C (HF+annealed) or hydrosilylation (HF+hydrosilylated), where 1-octadecene has been covalently bound to the H-terminated Si surface in a thermally induced reaction at 200 °C. Besides the excellent reduction of the number of defects per Si-nc by up to two orders of magnitude, these treatments are particularly promising as they simultaneously tune the surface of the Si-ncs, e.g., an efficient oxide removal and the attachment of functional organic groups. For a deeper understanding we have compared these results with those obtained for the individual process steps, namely only HF etching and only vacuum annealing. Moreover, in extension to recent studies on vacuum annealing,[24] we achieved a detailed knowledge for the choice of various annealing parameters, such as annealing time or

S. Niesar, Dr. A. R. Stegner, N. Erhard, Dr. M. Hoeb, Dr. A. Baumer, Prof. Dr. M. S. Brandt, Prof. Dr. M. Stutzmann
Walter Schottky Institut
Technische Universität München
Am Coulombwall 4, 85748 Garching, Germany
E-mail: niesar@wsi.tum.de; brandt@wsi.tum.de
Dr. R. N. Pereira
Departamento de Física and I3N
Universidade de Aveiro, 3810-193 Aveiro, Portugal
Dr. H. Wiggers
Institut für Verbrennung und Gasdynamik and CENIDE
Center of Nanointegration Duisburg-Essen
Universität Duisburg-Essen, Lotharstr. 1, 47048 Duisburg, Germany

DOI: 10.1002/adfm.201101811

external environment. With regard to the improvement of Si-ncs towards future applications, we show a strongly enhanced electrical conductivity measured on thin films of HF+annealed and of only annealed Si-ncs in comparison to films of H-terminated and of untreated Si-ncs, respectively. Moreover, we also address the stability of the defect reduction upon air exposure. The density of defects is found to be nearly unchanged on a timescale of more than one year for the combined treatments HF+annealing and HF+hydrosilylation. HF+hydrosilylated Si-ncs additionally show a good stability against reoxidation in air which enables the handling of these Si-ncs under ambient conditions.

2. Experimental Results and Discussion

2.1. Optimization of Low-Temperature Annealing Conditions

In recent studies, we have shown that vacuum annealing of Si-ncs at 200 °C for 2 h leads to a significant reduction of the Si-db density.[24] As the conditions described there have not been optimized in terms of annealing time and annealing atmosphere and might not be applicable during the preparation of electronic devices or in surface functionalization processes of the Si-ncs, we start this work by the presentation of a more detailed study of the required annealing conditions.

Figure 1 shows EPR spectra of Si-nc powder samples (a) in the as-grown state and after additional 70 h of storage in vacuum, as well as (b) after annealing at 200 °C for 2 h in vacuum, air, and inert gas (Ar) atmosphere. The term "as-grown" refers to Si-ncs without further treatment after synthesis which are oxidized during storage at ambient atmosphere and room temperature. The average diameter d of the Si-ncs, which is defined as the diameter d_{BET} determined by the Brunauer-Emmet-Teller method minus twice the average oxide thickness of 1.4 nm,[25] is 13 nm. All spectra are normalized to the sample mass. The as-grown signal shows a broad asymmetric resonance centered at $g \approx 2.004–2.006$. As described in Ref. [24], this spectrum can be assigned to a superposition of two Si-db defect species, namely P_b and D centers. The P_b centers are Si-dbs located directly at the interface between the crystalline Si-nc core and the native oxide shell while the D centers are Si-dbs that are not located at the outermost shell of the Si-nc core (cf. inset in Figure 1).[26–28]

From a comparison of the spectra in Figure 1a, we find that storage in vacuum for 70 h at room temperature alone is not sufficient to lead to a significant reduction of the Si-db density, which confirms that the defect reduction effect previously reported[24] is temperature-related. As can be seen in Figure 1b, annealing in air causes only a slight improvement of the defect density, while an effect similar to annealing in vacuum can be achieved by annealing in argon atmosphere. Therefore, we conclude that humidity and the presence of oxygen negatively affect the reduction of the Si-db density by low-temperature annealing.

In order to optimize the vacuum annealing process with respect to the annealing time, we have investigated the change of the surface Si-db density $[\text{Si-db}]_{surface}$ for 13 nm Si-ncs as a function of the annealing time at different annealing

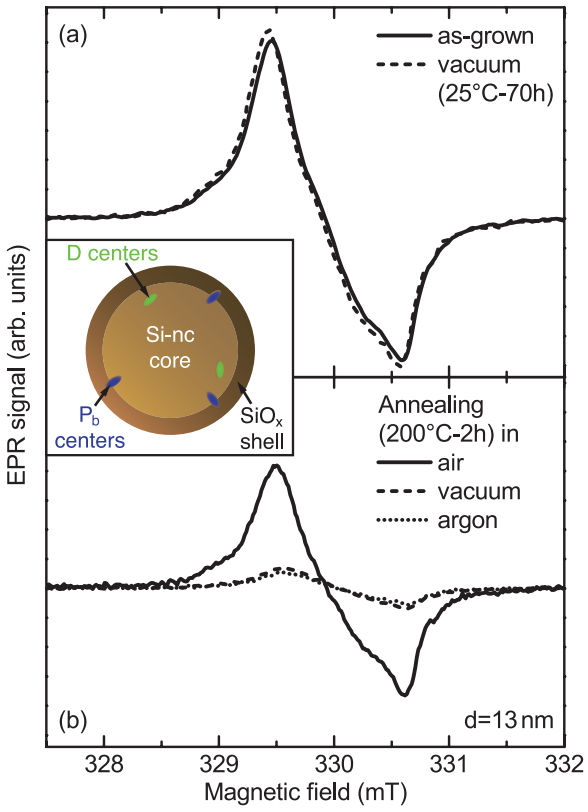

Figure 1. EPR spectra of Si-nc powder samples (d = 13 nm) a) in the as-grown state (solid line) and after storage in vacuum for 70 h (dashed line), as well as b) after annealing at 200 °C for 2 h in different gas atmospheres: air (solid line), vacuum (dashed line), and argon (dotted line). The inset shows a schematic image of a spherical Si-nc which is surrounded by an amorphous oxide shell. In addition, the two main Si-db species, namely P_b and D centers, are schematically shown.

temperatures of 200 °C, 250 °C and 350 °C. The data of these experiments are shown in **Figure 2**. As a reference, the dashed line indicates the as-grown value of $[\text{Si-db}]_{surface} = 7 \times 10^{11}$ cm^{-2} which has been determined from the corresponding spectrum in Figure 1a and the number of spins was normalized to the total internal surface area of the crystalline core. This is consistent with the previously reported value of 5×10^{11} cm^{-2} averaged over different Si-nc diameters.[25] For annealing at 200 °C, we find that an annealing time of 20 min is sufficient to achieve the maximum defect reduction reported in our previous work dedicated exclusively to annealing for 2 h.[24] To ensure that we always reach the saturation level for temperature treatments at 200 °C, in all experiments described below we have carried out the 200 °C annealings for 30 min. For 250 °C, the best value of 1×10^{11} cm^{-2} is already reached after a 10 min annealing. This is consistent with the fact that faster reaction dynamics are expected for higher temperatures as described by the Arrhenius equation.[29]

When the annealing temperature is further increased, the defect reduction starts to compete with the desorption of hydrogen passivating the Si-nc surfaces. For an annealing of 2 h, previous studies indicate that the two effects cancel out at a temperature of approx. 330 °C.[24,30] Therefore, we have

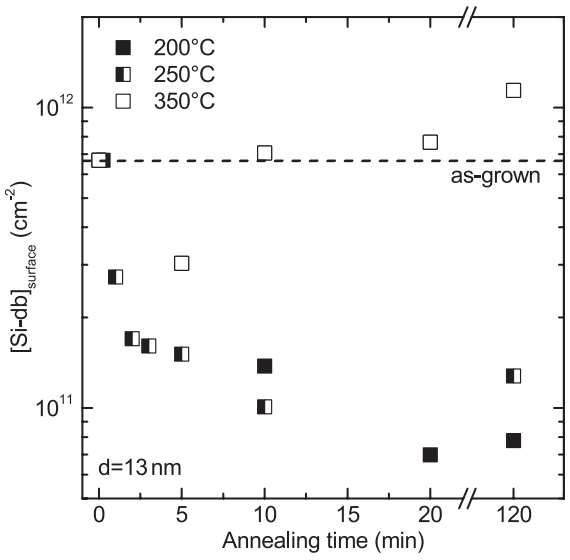

Figure 2. Surface Si-db density for as-grown Si-ncs (d = 13 nm) after annealing in vacuum at different temperatures and for different times. As a reference, the Si-db level for as-grown Si-ncs is shown.

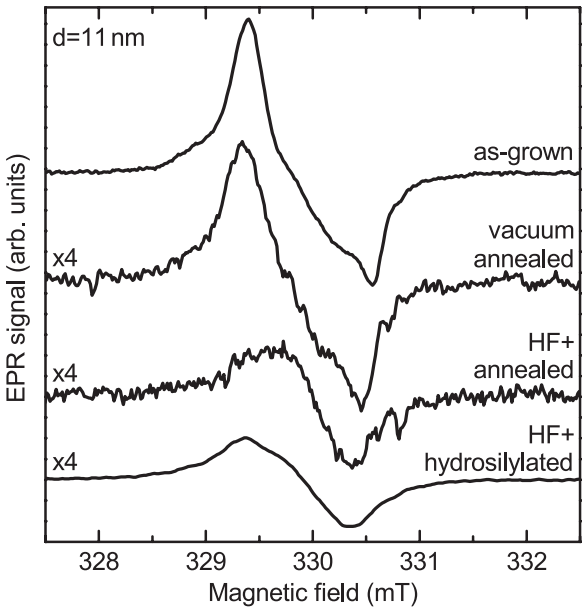

Figure 3. Comparison of a typical EPR spectrum for as-grown Si-ncs with a mean particle diameter of 11 nm with the corresponding spectra measured after vacuum annealing, HF+annealing, and HF+hydrosilylation.

investigated the annealing dynamics at a temperature of 350 °C where the hydrogen desorption slightly dominates. While for a short 5 min treatment $[Si\text{-}db]_{surface}$ is reduced by a factor of 2, already after 10 min the passivation effect and the desorption of hydrogen cancel each other and a Si-db density similar to the as-grown value is measured. For longer annealing times, the desorption of hydrogen becomes dominant. We observe a saturation of the defect density after 40–50 min (not shown) at $[Si\text{-}db]_{surface} = 1.1 \times 10^{12}$ cm^{-2}. The initial decrease of $[Si\text{-}db]_{surface}$ shows that the effect leading to a defect reduction has a significantly lower time constant than the hydrogen desorption.

2.2. Influence of Post-Growth Treatments on the Si-db Density

Now, we show the effect of different post-growth treatments on the number of Si-db defects for a wide range of Si-nc sizes. In particular, we concentrate on the combined treatments HF+annealing and HF+hydrosilylation. To investigate the effect of each treatment step in detail, we also analyse the properties of only HF etched and only annealed Si-ncs. In **Figure 3**, a typical EPR spectrum of as-grown Si-ncs with a diameter of 11 nm normalized to the sample mass is compared with the spectra of vacuum annealed, HF+annealed, and HF+hydrosilylated Si-ncs. While annealing in vacuum alone reduces $[Si\text{-}db]_{surface}$ from 3.5×10^{11} cm^{-2} to 1×10^{11} cm^{-2} by a factor of 3.5, HF+hydrosilylation as well as HF+annealing diminishes the number of defects by a factor of 10. The data show that the reduction of the defect density for the HF+hydrosilylated Si-ncs is as good as for the HF+annealed Si-ncs. This can be understood by the fact that the hydrosilylation process is thermally activated at 200 °C and carried out under argon atmosphere which leads to similar results as annealing in vacuum as concluded above (cf. Figure 1). The change of the line shape measured after the different treatments indicates that the relative contribution of the P_b centers has decreased for HF+hydrosilylated Si-ncs with respect to the as-grown Si-ncs. For HF+annealed Si-ncs, this has already been observed in Ref. [24]. The feature at 330.7 mT in the spectrum of the HF+annealed Si-ncs is a background signal of the resonator. It is only detected for samples with a low signal intensity, which is here caused by the relatively low defect density and low sample mass used.

To get a deeper understanding of the location of the defects in the Si-ncs, in **Figure 4**, we compare the number of Si-dbs per particle, $N_{Si\text{-}db}$, as a function of the particle diameter d in the range from 2 nm to 45 nm after the following treatments: vacuum annealing, HF etching, HF+annealing, and HF+hydrosilylation. The number of particles in our sample, which is needed for the calculation of $N_{Si\text{-}db}$, has been determined by dividing the total mass of the sample by the average mass of an individual Si-nc. The latter was calculated assuming a spherical Si-nc with diameter d_{BET} or d for Si-ncs with or without HF treatment, respectively. As expected, $N_{Si\text{-}db}$ decreases with decreasing particle diameter for as-grown Si-ncs (filled squares) and for all treatments. Among all treatments studied, HF etching alone (half-filled circles) leads to the smallest improvement of $N_{Si\text{-}db}$ as it only removes one defect contribution, i.e. the P_b centers, which are directly located at the Si/SiO_2 interface.[24] Annealing in vacuum alone already yields a slightly lower $N_{Si\text{-}db}$ for all particle diameters investigated. Here, on average, a reduction of $N_{Si\text{-}db}$ of a factor of 5 is found. Except for the largest Si-ncs, HF+annealing (open rhombs) and HF+hydrosilylation (open stars) lead to the best improvement of $N_{Si\text{-}db}$ by more than one order of magnitude. Moreover, we observe that the relative decrease of $N_{Si\text{-}db}$ induced by the treatments that include an HF etching step becomes stronger for smaller particle diameters.

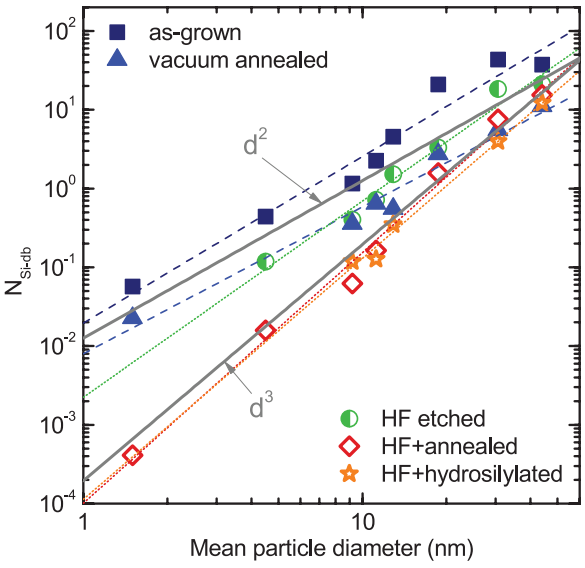

Figure 4. Number of defects per particle as a function of the mean particle diameter for as-grown and differently treated Si-ncs. All treatments, which include an HF etching step, are marked by open or half-filled symbols and the corresponding power law fits of the size dependence are depicted as dotted lines. The dashed lines refer to the fits for as-grown and vacuum annealed Si-ncs. For comparison, the solid lines show d^2 and d^3 power laws for $N_{Si\text{-}db}$.

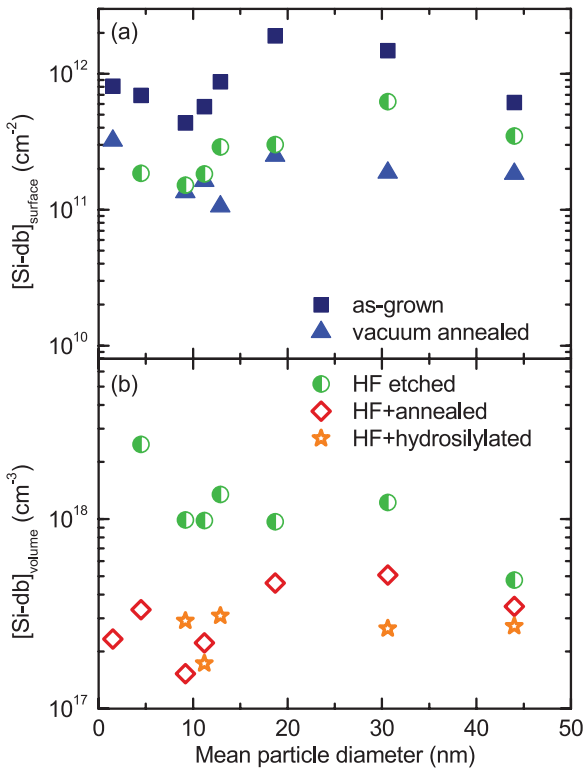

Figure 5. a) Surface Si-db density as a function of the mean particle diameter for as-grown, vacuum annealed, and HF etched Si-ncs. b) Volume Si-db density for Si-ncs after HF etching, HF+annealing as well as HF+hydrosilylation.

To quantitatively assess the differences in the size dependences of $N_{Si\text{-}db}$ for Si-ncs with a native oxide and HF etched Si-ncs, we have analyzed their scaling behavior. In the double logarithmic plot of Figure 4, the corresponding linear fits of the as-grown and vacuum annealed data are shown as dashed lines. The dotted lines correspond to fits of the measurements on Si-ncs that were subjected to treatments that include an HF etching step. For comparison, the solid lines indicate d^2 and d^3 power laws. While the unetched Si-ncs are in good agreement with a d^2 power law, the HF etched samples exhibit a stronger dependence on the diameter. The HF etched Si-ncs scale with $d^{2.5}$, HF+annealed and HF+hydrosilylation Si-ncs have a d^3 dependence. We conclude that the consideration of a surface Si-db density $[Si\text{-}db]_{surface}$ is only reasonable for Si-ncs with a native oxide, since for these Si-ncs the dominant part of the defects are located at the surface or in surface-near atomic layers. However, for Si-ncs that were subjected to treatments that include an HF etching step, the concept of the surface-related $[Si\text{-}db]_{surface}$ is no longer appropriate as the major part of the surface Si-dbs is removed by the HF treatment. Instead, the d^3 power law suggests that a volume Si-db defect density $[Si\text{-}db]_{volume}$ should be considered. This conclusion is in agreement with the different lineshapes of the resonances shown in Figure 3.

In **Figure 5**, the classification into surface and volume defect densities has been applied for all particles sizes and treatments. HF etched Si-ncs scaling with $d^{2.5}$ have been included in both datasets. For as-grown Si-ncs, an average value of $[Si\text{-}db]_{surface} = 7 \times 10^{11}$ cm^{-2} can be determined. This is in good agreement with typical literature values of 10^{12} cm^{-2} for bulk Si/SiO_2 interfaces[31] as well as with the average value of 5×10^{11} cm^{-2} measured on similar Si-ncs also synthesized in a microwave plasma reactor.[25] After HF etching, the average surface and volume Si-db densities are ~2×10^{11} cm^{-2} and 9×10^{17} cm^{-3}, respectively. For HF+annealing and HF+hydrosilylation, an average $[Si\text{-}db]_{volume} = 3 \times 10^{17}$ cm^{-3} is reached.

2.3. Stability of Defect Reduction Upon Air Exposure

2.3.1. FTIR Measurements: Oxidation Dynamics

For applications, it is of importance to gain a detailed knowledge about the stability of the treated Si-ncs upon air exposure. Therefore, to study surface chemistry, we have performed Fourier transform infrared (FTIR) spectroscopy on thin films of Si-ncs ($d = 44$ nm). In **Figure 6**, we compare spectra for all treatments, measured directly after film preparation (solid lines), with those measured after one week (dashed lines) and two weeks (dotted lines) of storage in air. All spectra were normalized to the respective sample thickness.

In the FTIR spectra of the as-grown Si-ncs, a large signal at ~1100 cm^{-1} is observed which can be attributed to the stretching mode of Si-O-Si bonds in the surface oxide of the Si-ncs.[32,11] Moreover, the measurements display lines around 2254 cm^{-1} and 880 cm^{-1} originating from the Si-H stretching and wagging of O_3-Si-H units and a band at ~2115 cm^{-1} due to H stretching in Si_{4-x}-Si-H_x ($x = 1, 2, 3$) bonds.[33] The initial FTIR spectrum

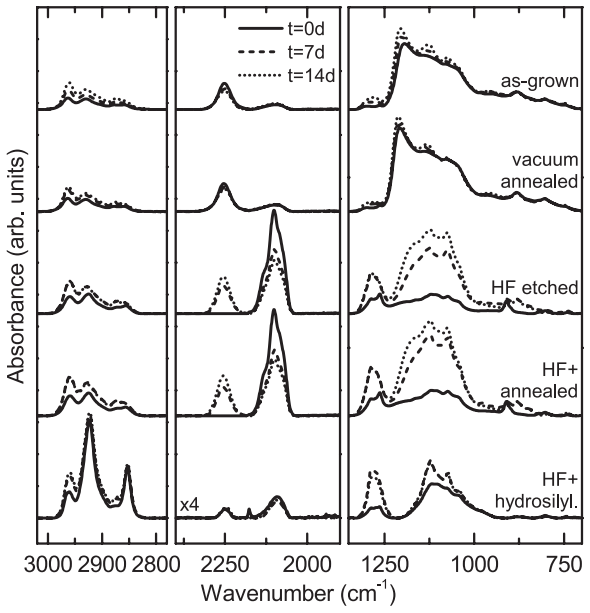

Figure 6. FTIR spectra of Si-nc films ($d = 44$ nm) with an average thickness of ~1 µm: as-grown, after vacuum annealing, HF etching, HF+annealing, and HF+hydrosilylation. The dashed and dotted lines show the spectra measured after one and two weeks of storage in ambient atmosphere.

of the vacuum annealed Si-nc film essentially resembles the spectrum of the as-grown Si-nc films.

An efficient oxide removal is reflected by the much lower signal intensity of the oxygen-related peaks (Si-O-Si, O_3-Si-H) in the spectrum which is recorded directly after HF etching. At the same time, a strong increase of the Si-H stretching mode at 2115 cm^{-1} is observed and the H scissors mode of Si_2-Si-H_2 at 910 cm^{-1} appears[34] indicating that the surface oxide of the Si-ncs has been replaced by H termination. Moreover, a further peak at 1285 cm^{-1} is observed which could be related to the CH_3 symmetric deformation mode due to a Si-CH_3 group.[35] A similar behavior has already been reported for etched porous silicon where the appearance of C-H peaks was related to HF-ethanol residues,[36] which in our case could have formed due to the rinsing of the Si-ncs with ethanol after HF etching. As can be seen, a subsequent vacuum annealing of the HF etched Si-nc film does not lead to further changes of the IR signals observed. In combination with the similarity between the spectra of the as-grown and vacuum annealed Si-nc films, we conclude that vacuum annealing at 200 °C in general does not lead to a significant change of the IR absorbance spectrum. This particularly implies that no significant amount of hydrogen is lost from the surface.

For HF+hydrosilylated Si-ncs, we additionally observe typical strong peaks in the region of 2850 cm^{-1}, 2920 cm^{-1} and 2960 cm^{-1} which are assigned to different symmetric and asymmetric C-H_x stretching vibrations.[37] In combination with the weaker C-H_x deformation (bending) bands at 1330–1490 cm^{-1} (not shown), this is consistent with the successful attachment of 1-octadecene to the Si-ncs. Our findings are in line with other works on the hydrosilylation of silicon nanoparticles.[20,23] The weak intensity of the methyl stretching modes in the spectra of non-hydrosilylated Si-ncs is most likely due to atmospheric carbon contamination in our FTIR spectrometer. Comparing the spectra recorded on HF etched and HF+hydrosilylated Si-ncs, a similar reduction of the oxygen-related peaks compared to the spectrum of the as-grown Si-ncs is found. Furthermore, the amount of Si-H bonds is reduced for the case of the HF+hydrosilylated Si-ncs due to the partial substitution of the hydrogen termination by octadecyl chains.

Now, we address the time evolution of the IR spectra observed after the different treatments. As can be seen in Figure 6, for as-grown and vacuum annealed Si-ncs, the observed absorbance bands are relatively stable after film deposition on a timescale of two weeks. Nevertheless, we observe a slight decrease of the peak at 2254 cm^{-1} (O_3-Si-H units), which is correlated with an increase of the Si-O-Si band around 1100 cm^{-1}. We attribute these variations to small changes in the oxide configuration and oxidation of Si-nc surfaces that have been newly exposed to air after the dispersion in the solution and film deposition processes. For the samples, where the native oxide has been removed by an HF etching step, the IR spectra show changes, in particular for the O_3-Si-H (2185–2325 cm^{-1}), Si_{4-x}-Si-H_x (2030–2175 cm^{-1}), and Si-O-Si (950–1235 cm^{-1}) bands. To illustrate the quantitative variation of these bands, we have plotted their intensities as a function of time in **Figure 7**, where we also include additional data points. For clarity, we have omitted some of the corresponding spectra in Figure 6.

For HF etched and HF+annealed Si-ncs, the signal intensities of the oxide-related peaks (Figure 7a and c) show an initial strong rise in the first two days after deposition, which is followed by a slower continuous increase. This is correlated with a decrease of the Si_{4-x}-Si-H_x signal (Figure 7b) showing the same dynamics. This time evolution indicates a slow reoxidation of the Si-nc surfaces in air on a timescale of several days. A similar behavior has been reported for the oxidation in silicon nano-/microcrystals,[38,39] small silicon particles,[40,41] silicon clusters,[42] and porous silicon.[43,44] Comparing the relative peak intensities of the oxide-related bands in the spectra of the as-grown and HF etched Si-nc films after 14 days of storage in air in Figure 6, we find that the structure of the oxide formed after HF etching slightly differs from the native oxide of the as-grown Si-ncs.

HF+hydrosilylated Si-ncs display a quite distinct behavior upon storage in air. For these Si-ncs, we observe only a weak initial increase of the Si-O-Si band which is followed by a plateau region without further oxidation. The Si_{4-x}-Si-H_x signal shows a correspondingly stable behavior. The increase of the O_3-Si-H signal measured for the HF etched and HF+annealed Si-ncs is not found. A similarly good stability can be reported for the C-H_x stretching vibrations at 2850 cm^{-1} and 2920 cm^{-1}. These observations indicate that the attached alkyl chains effectively hinder the reoxidation of the Si-nc surface. The small initial oxidation could originate from regions of the Si-nc surfaces where the functionalization process has been incomplete.

2.3.2. EPR Measurements: Stability of Defect Reduction

To address the question of how the evolution of the surface properties, discussed in the previous subsection, affects the number of defects per particle, we have monitored $N_{Si\text{-}db}$ for

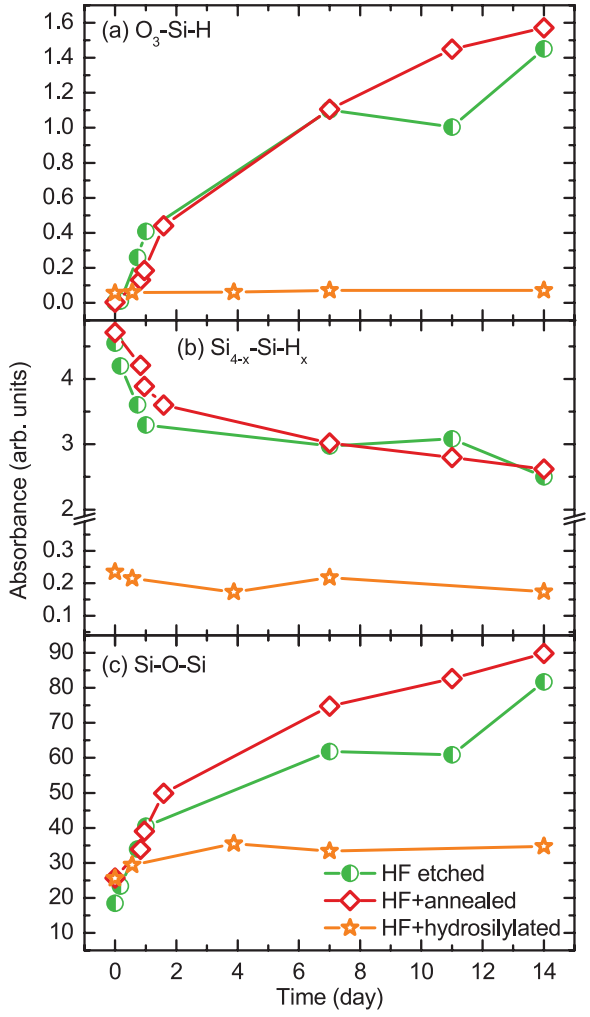

Figure 7. Normalized maximum absorbance values for all treatments for the FTIR peaks at a) 2185–2325 cm^{-1}, b) 2030–2175 cm^{-1} and c) 950–1235 cm^{-1}.

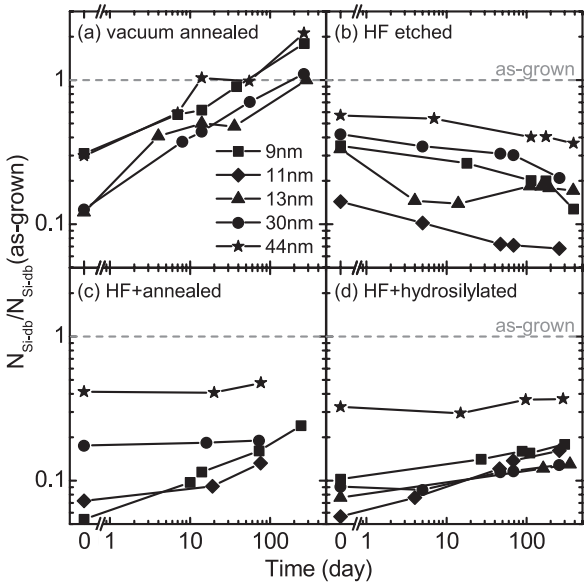

Figure 8. Evolution of the number of spins per particle for Si-ncs with different mean particle diameters after a) vacuum annealing, b) HF etching, c) HF+annealing, and d) HF+hydrosilylation. All data are normalized to the respective as-grown values.

all treatments and various Si-nc diameters on an air exposure timescale of several days to more than one year. The resulting data are summarized in **Figure 8**, where the different symbols indicate the different Si-nc diameters *d*. All data points were normalized to the respective as-grown value, N_{Si-db} (as-grown).

In Figure 8a, the evolution of N_{Si-db}/N_{Si-db} (as-grown) is shown for vacuum annealed Si-ncs. After one year, N_{Si-db} has increased by a factor of 5-10 and reaches the as-grown value independently of the Si-nc size. In Figure 4, we have observed, both for as-grown and annealed Si-ncs, that the amount of Si-db scales with d^2. We therefore expect a size-independent behavior which is in agreement with the defect recovery depicted here.

For HF etched Si-ncs, the time-dependent change of N_{Si-db}/N_{Si-db}(as-grown) is plotted in Figure 8b. The curves show that the number of defects is quite stable after HF etching on a long timescale. N_{Si-db} even improves by ~50% on average. This improvement is more strongly pronounced for the smaller Si-ncs. In view of the FTIR measurements, which clearly show a reoxidation of the HF etched Si-ncs in the first days, an enhancement of N_{Si-db} could have been expected due to the formation of interface defects,[39] in apparent contrast to our EPR results.

To learn more about the correlation between the defect density and the oxide growth, we have performed continuous EPR and FTIR measurements in the first week after sample preparation for HF etched Si-ncs (d = 11 nm) as shown in **Figure 9**a and b (filled squares), respectively. We compare the evolution of N_{Si-db} with the intensity of the Si-O-Si band around 1100 cm^{-1}, which is a measure for oxidation and has been determined by numerical integration of the absorbance spectrum in the range from 940–1250 cm^{-1}. Both datasets were normalized to the respective first experimental value recorded approx. one hour after stopping the etching process. We observe a logarithmic increase of the intensity of the oxide-related band in the IR measurements. This behavior is typical for the room-temperature oxidation kinetics of silicon surfaces and follows the Elovich equation.[39,45,46] N_{Si-db} rises in the first 16 h by a factor of 2.3. In the following 100 h, we observe a decrease of N_{Si-db} back to its initial value which is continued by a further decrease on the timescale of more than one year as shown in Figure 8b.

This behavior can be understood taking into account that EPR can monitor the formation of the Si/oxide interface which changes the amount of dangling bonds at the Si-nc surface.[39] However, when the oxidation proceeds, a maximum amount of Si-dbs is reached when the surface is fully covered with the first oxide layer. The following reduction of the Si-db defects indicates a subsequent reconstruction of the interface, which results in more saturated bonds. Importantly, N_{Si-db}/N_{Si-db} (as-grown) measured after one year (cf. Figure 8b) suggests

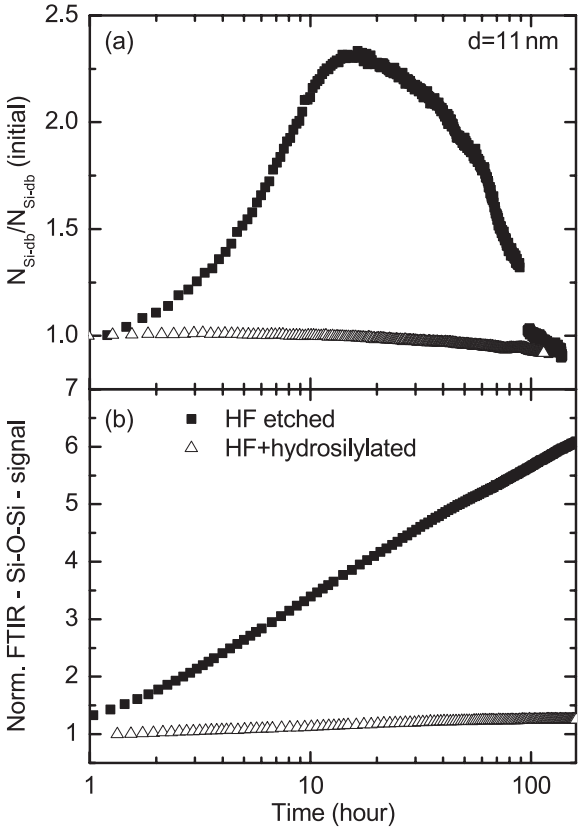

Figure 9. a) Change of the number of defects per particle for HF etched and hydrosilylated Si-ncs ($d = 11$ nm) in the first days after sample preparation and b) direct comparison to the oxygen-related Si-O-Si FTIR-signal ~1100 cm^{-1} which is a measure for the oxidation.

that the interface formed on the HF etched surface is of better quality than the native Si/SiO_x interface of the as-grown Si-ncs.

While the HF+annealed Si-ncs show a similar behavior as the HF etched Si-ncs, as far as the FTIR data are concerned, the time evolution of N_{Si-db}, shown in Figure 8c, strongly differs. Instead of the long-term decrease discussed above for the HF etched Si-ncs, we observe a small increase for all particle diameters. We explain this behavior by a superposition of the changes of N_{Si-db} induced by the reoxidation (cf. Figure 8b) and by the recovery of the defects obtained after vacuum annealing (cf. Figure 8a). The resulting relative rise in N_{Si-db} is more pronounced for the smaller Si-ncs for which also the initial relative defect reduction was the strongest as discussed in the context of Figure 4. However, we note that N_{Si-db} significantly stays below the as-grown value for all of the samples, which makes this treatment particularly promising for applications.

In analogy to HF+annealed Si-ncs, N_{Si-db} slightly increases over time for the HF+hydrosilylated Si-ncs due to a partial decrease of the defect reduction effect expected for the hydrosilylation-inherent annealing step (cf. Figure 8d). Nonetheless, we find an overall good stability of N_{Si-db} on a low level in relation to the as-grown value. The HF+hydrosilylated Si-ncs have the additional advantage that no surface oxide shells are formed. Besides the long-term stability of the oxygen-related IR bands (cf. Figure 7), this is also evidenced by the direct comparison of the Si-db EPR signal strength and the intensity of the Si-O-Si IR signal during the first ~100 h shown in Figure 9 (open triangles). There, the increase of N_{Si-db} discussed for the HF etched Si-ncs is not found and the Si-O-Si IR signal changes at a much lower rate before it saturates at ~100 h which indicates that the formation of a defective Si/SiO_x interface is strongly suppressed.

2.4. Influence on the Electrical Conductivity

An important question for (opto)electronic applications of the Si-ncs is whether the defect reduction also improves the electrical conductivity σ of Si-nc networks. Therefore, we have studied the influence of vacuum annealing (200 °C, 30 min) on the conductivity of as-grown and HF etched Si-nc films. For all measurements, which have been performed in situ in our annealing setup, a voltage of 1 V was applied to the contact grid on which the Si-nc film was deposited and the current before the annealing and one hour after the annealing was recorded, when the sample temperature had returned to room temperature. **Figure 10** shows the relative conductivity change induced by the annealing for as-grown (filled triangles) as well as HF etched Si-nc films (open rhombs) as a function of the Si-nc diameter. For both cases, the conductivity after annealing is significantly enhanced. We observe that the annealing of as-grown Si-nc films leads to a nearly size-independent improvement of a factor of ~20. For HF etched Si-nc films, we find a strong size dependence and a maximum improvement of the conductivity by more than two orders of magnitude for Si-ncs with $d < 20$ nm, reaching a maximum increase of more than 400.

Comparing the conductivity results with the defect reduction, which was determined by EPR and discussed in the context of Figure 4, we find a good agreement in various respects. First, the reduced number of Si-dbs is also reflected in an improved conductivity. Further, as the number of spins shows the same

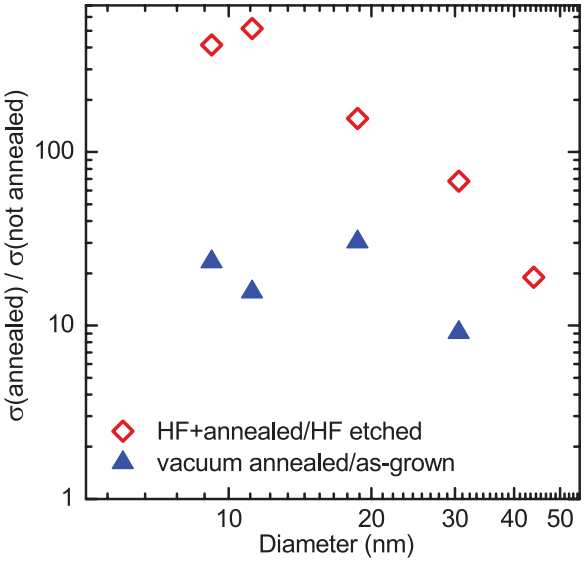

Figure 10. Ratio of the conductivity after and before vacuum annealing of as-grown (filled triangles) and HF etched (open rhombs) Si-nc films as a function of the particle diameter.

size dependence for both, as-grown and vacuum annealed Si-ncs, we expect a size-independent conductivity improvement from as-grown to annealed Si-nc films. This is consistent with the data shown in Figure 10. For HF etched Si-ncs, a subsequent vacuum annealing step leads to a relatively stronger defect reduction for smaller Si-ncs. This finding is in line with the size dependence of the conductivity improvement which we observe for the HF+annealed Si-nc films and clearly identifies the Si-db defects as transport-influencing trapping centers.

3. Summary

In this work, we have reported different routes to improve the defect properties in freestanding Si-ncs grown from the gas phase which offer large potential for future application in photovoltaics, thermoelectrics, and electronics. We found that HF etching of the Si-ncs combined with a subsequent annealing step at 200 °C under vacuum or inert gas atmosphere strongly reduces the concentration of Si dangling bond defects by up to two orders of magnitude for Si-ncs with diameters between 2 nm and 45 nm. Similar results are obtained for HF etched Si-ncs which were surface functionalized via a thermally induced hydrosilylation process, where the process parameteres were adjusted to the requirements established for the only annealing treatment. Electrical measurements performed on thin Si-nc films reveal that HF+annealing also leads to a significantly enhanced electrical conductivity in comparison to only HF etching indicating that the reduction of the number of defects and of the transport limiting oxide layers are major steps towards more efficient devices. Recent studies have shown that these post-growth treatments indeed have the potential to strongly increase the efficiency of hybrid P3HT/Si-ncs solar cells.[15] Moreover, with regard to such applications we addressed the question of reoxidation of the Si-nc surface and stability of the defect reduction over time. Here, we demonstrate that the number of defects only slightly changes on a timescale of one year and stays significantly below the as-grown level for all treatments which include an HF etching step when the Si-ncs are stored in air. The attachment of functional groups (HF+hydrosilylation) additionally hinders the reoxidation of the Si-ncs in air. This illustrates the possibility of a simultaneous tuning of the surface termination and reduction of the defect density which is highly beneficial for future advances in the surface design of the Si-ncs and for applications in functional devices.

4. Experimental Section

A low-pressure microwave plasma reactor was used to synthesize the nominally undoped Si-ncs investigated in this work via decomposition of silane.[32,47] The gas flow, the pressure and the relative concentrations of the precursor gases SiH_4, Ar and H_2 determine the diameter d of the Si-ncs, which can be selected between 2 nm and 45 nm. From transmission electron microscope images it is known that the Si-ncs have a spherical shape with a mostly single crystalline core.[41] After exposure to air, a native oxide shell with an average thickness of 1.4 ± 0.4 nm is formed.[25] We define the average Si-nc diameter d of our Si-nc samples as the diameter d_{BET} determined by the Brunauer-Emmet-Teller method[48] minus twice the average oxide thickness. We refer to Si-ncs which are oxidized by storing at room temperature and ambient atmosphere and measured without further treatment after synthesis as "as-grown" Si-ncs.

To remove the native oxide shell, the Si-ncs were etched in diluted HF (10% in water) for three minutes and subsequently rinsed with ethanol. The annealing experiments were performed in an evacuated quartz tube with a base pressure of $<10^{-7}$ mbar which was equipped with a resistively heated tube oven. For the determination of the optimal process parameters, some samples were annealed in air or under argon atmosphere, where the residual content of oxygen and water is below 1 ppm.

Thermally induced hydrosilylation was used as the chemical route to attach 1-octadecene to the Si-ncs in accordance with the process published for bulk Si.[49] Immediately after etching of the Si-ncs with hydrofluoric acid, the resulting H-terminated Si-ncs were added to neat 1-octadecene, which was dried over CaH_2 for 2 h at 130 °C and distilled under vacuum (10^{-2} mbar) at 130–140 °C. Then, the mixture was stirred under argon atmosphere at 200 °C for 1 h and subsequently distilled at a temperature of 150 °C to remove the residual octadecene. The remaining functionalized Si-ncs were washed several times with hexane.

For EPR measurements, the etched and hydrosilylated Si-ncs were dried by centrifuging the Si-nc dispersion. Subsequently, the Si-nc powder was filled into quartz sample tubes. The weight of the Si-ncs in the samples was determined with a high-precision scale (Sartorius R200D). A continuous wave X-band spectrometer (Bruker) with a TE_{102} cavity was used for the measurements. The EPR signal was recorded using lock-in technique with magnetic field modulation at 100 kHz. All measurements were performed at room temperature. The number of Si-dbs were determined via double numerical integration of the corresponding EPR signals and comparison with the signal intensity of a 2,2-diphenyl-1-picrylhydrazyl reference sample.

The FTIR spectra were detected with a Bruker Vertex 70v Fourier-transform spectrometer in reflection mode with a resolution of 2 cm^{-1}. For this purpose, the particles were dispersed in ethanol or hexane, depending on their previous treatment, and spin-coated onto flexible Kapton polyimide substrates with a reflecting layer of thermally evaporated gold. The resulting ~1 μm thick Si-nc films were measured at room temperature in a probe chamber with a base pressure of 10^{-3} mbar. Baseline measurements were performed on a blank gold-covered Kapton substrate.

For electrical measurements ~500 nm thick Si-nc films were spin-coated onto 2 mm × 2 mm interdigit Au contact grid structures (grid spacing 10 μm) deposited on Kapton polyimide substrates.

Acknowledgements

This work is funded by the Karl-Max von Bauernfeind-Verein and the International Graduate School "Material Science for Complex Interfaces (CompInt)" of the Technische Universität München, by CRUP-DAAD via an "Acção Integrada Luso-Alemã", by FCT/I3N via the HybridSolar project, by the DFG via SFB 563, Teilprojekt B2 and by the European Union and the Ministry of Innovation, Science and Research of the German State of North Rhine-Westphalia in the framework of an Objective 2 Programme (European Regional Development Fund, ERDF).

Received: August 4, 2011
Published online: January 23, 2012

[1] W. U. Huynh, J. J. Dittmer, A. P. Alivisatos, *Science* **2002**, *295*, 2425.
[2] M. S. Dresselhaus, G. Chen, M. Y. Tang, R. Yang, H. Lee, D. Wang, Z. Ren, J.-P. Fleurial, P. Gogna, *Adv. Mater.* **2007**, *19*, 1043.
[3] S. A. McDonald, G. Konstantatos, S. Zhang, P. W. Cyr, E. J. D. Klem, L. Levina, E. H. Sargent, *Nature Mat.* **2005**, *4*, 138.
[4] R. Lechner, H. Wiggers, A. Ebbers, J. Steiger, M. S. Brandt, M. Stutzmann, *Phys. Stat. Sol. RRL* **2007**, *1*, 262.

[5] Z. C. Holman, C.-Y. Liu, U. R. Kortshagen, *Nano Lett.* **2010**, *10*, 2661.
[6] U. Kortshagen, *J. Phys. D: Appl. Phys.* **2009**, *42*, 113001.
[7] A. Gupta, M. T. Swihart, H. Wiggers, *Adv. Funct. Mater.* **2009**, *19*, 696.
[8] S. Niesar, R. Dietmueller, H. Nesswetter, H. Wiggers, M. Stutzmann, *Phys. Stat. Sol. A* **2009**, *206*, 2775.
[9] A. Baumer, M. S. Brandt, M. Stutzmann, H. Wiggers, US Patent Application 2010/0221544, **2010**.
[10] M. A. Rafiq, Y. Tsuchiya, H. Mizuta, S. Oda, S. Uno, Z. A. K. Durrani, W. I. Milne, *Appl. Phys. Lett.* **2005**, *87*, 182101.
[11] A. R. Stegner, R. N. Pereira, K. Klein, R. Lechner, R. Dietmueller, M. S. Brandt, M. Stutzmann, *Phys. Rev. Lett.* **2008**, *100*, 026803.
[12] X. Zhou, K. Usami, M. A. Rafiq, Y. Tsuchiya, H. Mizuta, S. Oda, *J. Appl. Phys.* **2008**, *104*, 024518.
[13] X. Zhou, K. Uchida, H. Mizuta, S. Oda, *J. Appl. Phys.* **2009**, *105*, 124518.
[14] D. Herrmann, S. Niesar, C. Scharsich, A. Koehler, M. Stutzmann, E. Riedle, *J. Am. Chem. Soc.* **2011**, *133*, 18220.
[15] S. Niesar, W. Fabian, N. Petermann, D. Herrmann, E. Riedle, H. Wiggers, M. S. Brandt, M. Stutzmann, *Green* **2011**, **1**, 339.
[16] X. Michalet, F. F. Pinaud, L. A. Bentolila, J. M. Tsay, S. Doose, J. J. Li, G. Sundaresan, A. M. Wu, S. S. Gambhir, S. Weiss, *Science* **2005**, *307*, 538.
[17] R. D. Tilley, J. H. Warner, K. Yamamoto, I. Matsui, H. Fujimori, *Chem. Commun.* **2005**, *1833*.
[18] F. Hua, F. Erogbogbo, M. T. Swihart, E. Ruckenstein, *Langmuir* **2006**, *22*, 4363.
[19] J. G. C. Veinot, *Chem. Commun.* **2006**, 4160.
[20] M. Rosso-Vasic, E. Spruijt, B. van Lagen, L. de Cola, H. Zuilhof, *Small* **2008**, *10*, 1835.
[21] J. Nelles, D. Sendor, F.-M. Petrat, U. Simon, *J. Nanopart. Res.* **2010**, *12*, 1367.
[22] A. Shiohara, S. Hanada, S. Prabakar, K. Fujioka, T. H. Lim, K. Yamamoto, P. T. Northcote, R. D. Tilley, *J. Am. Chem. Soc.* **2010**, *132*, 248.
[23] J. A. Kelly, A. M. Shukaliak, M. D. Fleischauer, J. G. C. Veinot, *J. Am. Chem. Soc.* **2011**, *133*, 9564.
[24] S. Niesar, A. R. Stegner, R. N. Pereira, M. Hoeb, H. Wiggers, M. S. Brandt, M. Stutzmann, *Appl. Phys. Lett.* **2010**, *96*, 193112.
[25] A. R. Stegner, R. N. Pereira, R. Lechner, K. Klein, H. Wiggers, M. Stutzmann, M. S. Brandt, *Phys. Rev. B* **2009**, *80*, 165326.
[26] E. H. Poindexter, P. J. Caplan, B. E. Deal, R. R. Razouk, *J. Appl. Phys.* **1981**, *52*, 879.
[27] A. Stesmans, V. V. Afanas'ev, *J. Appl. Phys.* **1998**, *83*, 2449.
[28] M. Stutzmann, D. K. Biegelsen, *Phys. Rev. B* **1989**, *40*, 9834.
[29] A. Stesmans, *Phys. Rev. B* **2000**, *61*, 8393.
[30] P. Gupta, V. L. Colvin, S. M. George, *Phys. Rev. B* **1988**, *37*, 8234.
[31] N. M. Johnson, W. B. Jackson, M. D. Moyer, *Phys. Rev. B* **1985**, *31*, 1194.
[32] J. Knipping, H. Wiggers, B. Rellinghaus, P. Roth, D. Konjhodzic, C. Meier, *J. Nanosci. Nanotechnol.* **2004**, *4*, 1039.
[33] G. Lucovsky, J. Yang, S. S. Chao, J. E. Tylor, W. Czubatyj, *Phys. Rev. B* **1983**, *28*, 3225.
[34] W. Theiss, *Surf. Sci. Rep.* **1997**, *29*, 91.
[35] N. B. Colthup, L. H. Daly, S. E. Wiberley, *Introduction to Infrared and Raman Spectroscopy*, Academic Press, Inc., San Diego **1990**.
[36] A. Borghesi, A. Sassella, B. Pivac, L. Pavesi, *Solid State Commun.* **1993**, *87*, 1.
[37] K. F. Voss, C. M. Forster, L. Smilowitz, D. Mihailovic, S. Askari, G. Srdanov, Z. Ni, S. Shi, A. J. Heeger, F. Wudl, *Phys. Rev. B* **1991**, *43*, 5109.
[38] S. Hayashi, S. Kawata, H. M. Kim, K. Yamamoto, *Jpn. J. Appl. Phys.* **1993**, *32*, 4870.
[39] R. N. Pereira, D. J. Rowe, R. J. Anthony, U. Kortshagen, *Phys. Rev. B* **2011**, *83*, 155327.
[40] R. Okada, S. Iijima, *Appl. Phys. Lett.* **1991**, *58*, 1662.
[41] R. N. Pereira, S. Niesar, W. B. You, A. F. da Cunha, N. Erhard, A. R. Stegner, H. Wiggers, M.-G. Willinger, M. Stutzmann, M. S. Brandt, *J. Phys. Chem. C* **2011**, *115*, 20120.
[42] M. F. Jarrold, U. Ray, K. M. Creegan, *J. Chem. Phys.* **1990**, *93*, 224.
[43] B. Hamilton, *Semicond. Sci. Technol.* **1995**, *10*, 1187.
[44] E. A. Petrova, K. N. Bogoslovskaya, L. A. Balagurov, G. I. Kochoradze, *Mater. Sci. Eng.* **2000**, *B69-70*, 152.
[45] G. F. Cerofolini, G. La Bruna, L. Meda, *Appl. Surf. Sci.* **1996**, *93*, 255.
[46] S. I. Raider, R. Flitsch, M. J. Palmer, *J. Electrochem. Soc.* **1975**, *122*, 413.
[47] C. Meier, S. Luettjohann, V. G. Kravets, H. Nienhaus, A. Lorke, H. Wiggers, *Physica E* **2006**, *32*, 155.
[48] S. Brunauer, P. Emmett, E. Teller, *J. Am. Chem. Soc.* **1938**, *60*, 309.
[49] M. R. Linford, P. Fenter, P. M. Eisenberger, C. E. D. Chidsey, *J. Am. Chem. Soc.* **1995**, *117*, 3145.